Int J CARS (2006) 1:23–31
DOI 10.1007/s11548-006-0001-4

ORIGINAL ARTICLE

3D segmentation of medical images using a fast multistage hybrid algorithm

Lixu Gu · Terry Peters

Abstract In this paper, we propose a fast multistage hybrid algorithm for 3D segmentation of medical images. We first employ a morphological recursive erosion operation to reduce the connectivity between the object to be segmented and its neighborhood; then the fast marching method is used to greatly accelerate the initial propagation of a surface front from the user defined seed structure to a surface close to the desired boundary; a morphological reconstruction method then operates on this surface to achieve an initial segmentation result; and finally morphological recursive dilation is employed to recover any structure lost in the first stage of the algorithm. This approach is tested on 60 CT or MRI images of the brain, heart and urinary system, to demonstrate the robustness of this technique across a variety of imaging modalities and organ systems. The algorithm is also validated against datasets for which "truth" is known. These measurements revealed that the algorithm achieved a mean "similarity index" of 0.966 across the three organ systems. The execution time for this algorithm, when run on a 550 MHz Dual PIII-based PC runningWindows NT, and extracting the cortex from brain MRIs, the cardiac surface from dynamic CT, and the kidneys from 3D CT, was 38, 46 and 23 s, respectively.

Keywords Image guided surgery · Recursive erosion · Fast marching · Morphological reconstruction · Recursive dilation · Similarity index

Introduction

One of the basic problems in medical imaging is to precisely segment structures of interest from a huge dataset, accurately represent them, efficiently visualize them and perform measurements appropriate for diagnosis, surgery and therapy guidance, or other applications [1,2]. Most current segmentation algorithms applied to medical imaging problems only detect the rough boundaries of the structures in two dimensions (2D), and as such do not satisfy the requirement of high accuracy required of many medical applications. The continuing evolution of computer-aided diagnosis, image-guided and robotically-assisted surgery, mandates the development of efficient, accurate three dimensional (3D) segmentation procedures.

Segmentation techniques can be divided into classes in many ways [3,4], according to different classification schemes, however model-based and region-based techniques represent the two main groups.

Model-based procedures include "snake" algorithms (deformable model, active contours etc.), as initially proposed by Kass et al. [5], and level set methods (aswell as fast marching methods), proposed by Osher and Sethian [6]. These techniques are based on deforming an initial contour or surface towards the boundary of the object to be detected. The deformation is obtained by minimizing a customized energy function such that its local minima are reached at the boundary of the desired structure. These algorithms are generally fast and efficient but the outcomes are often low in accuracy for the following reasons.

Since the stopping term of the deformation evolution depends on the image gradient flow being approximately zero, this often forces the contours to stop several voxels away from the desired boundary.Thus the active contour sometimes does not match the boundary of the structure accurately,

---

L. Gu
Computer Sciense, Shanghai Jiaotong University,
Shanghai, People's Republic of China

L. Gu (✉) · T. Peters
Imaging Research Laboratories, Robarts Research Institute,
London, Ontario Canada
E-mail: gu-lx@cs.sjtu.edu.cn

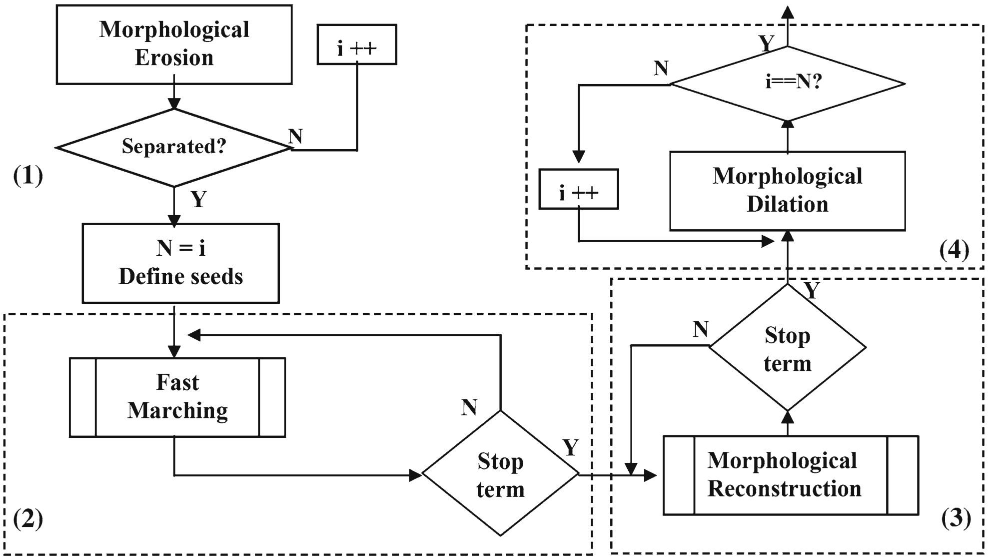

Fig. 1 Proposed multistage hybrid segmentation scheme. (1) Recursive erosion; (2) the fast marching method; (3) Morphological reconstruction; (4) recursive dilation

especially in regions with steep curvature and low gradient values.

Since a surface tension component is incorporated into the energy function to smooth the contour, it also prevents the contour fully propagating into corners or narrow regions. Increasing the number of the sample nodes along the contour can improve the situation, but at a significant increase in computational cost.

The existence of multiple minima and the selection of the elasticity parameters can affect the accuracy of the outcome significantly.

Region-based algorithms include region growing [7],morphological reconstruction [8] and watershed [9]. Since these procedures are generally based on neighborhood operations, and examine each pixel during the evolution of the edge, the outcomes are usually highly accurate. On the other hand, although there are several optimized algorithms in the literature [10,11], they are generally computationally intensive.

In this paper, we propose a new 3D hybrid segmentation algorithm, which works in a multistage manner to perform segmentations rapidly and precisely [12]. A flow chart of the algorithm is shown in Fig. 1. In the first stage, we employ a morphological recursive erosion to reduce the connectivity between the object and its neighboring tissues. Then a fast marching method is employed in the second stage to greatly accelerate the initial propagation from the user-defined seed structure to the vicinity of the boundary of object. In the third stage, we employ a morphological reconstruction algorithm [8] to refine the propagation to achieve a highly accurate boundary. At the end of the segmentation procedure, morphological recursive dilation is implemented, using the same number of iterations as recorded in stage one, to recover regions lost during the initial erosion, but at the same time avoiding re-connection to the surrounding structures. The segmented result may be presented to the user by volume rendering (ray casting) or surface rendering (matching cube) methods.

There are several segmentation algorithms described in the literature to facilitate medical image visualization and manipulation [13–21]. Most of them deal with medical images in a 2D manner, and are limited to particular application studies. Computational time is often not addressed. In contrast, our approach performs full 3D implementations, and is tested by a variety of application studies including neurological, cardiac and urinary tract datasets. We discuss the computational effort required for each of the three typical clinical scenarios.

The remainder of this paper is organized as follows. In the second section, we present a brief reviewof fast marching method and morphological reconstruction techniques, while third section describes our multistage hybrid segmentation algorithm. We demonstrate this algorithm in three study cases using neurological, cardiac and urinary tract datasets in the fourth section, and follow in the fifth section with a validation experiment using three 3D datasets. The robustness and accuracy of our approach are discussed in the last section.

Fast matching and morphological reconstruction

Level set and fast marching

The level set method [22] is an interface propagation algorithm that represents a curve as the zero level set of a function,

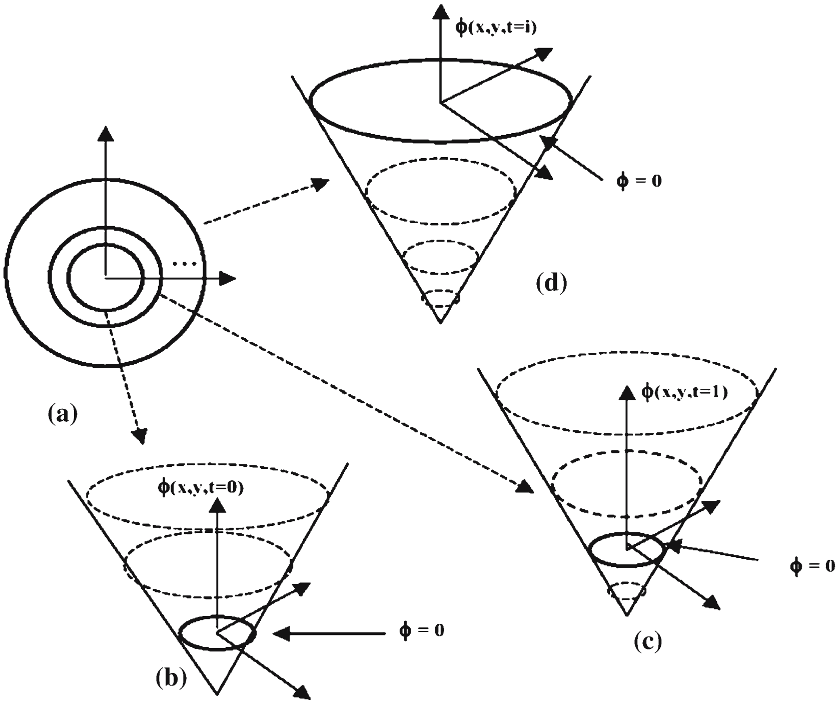

Fig. 2 Level set function and zero level set $\phi = 0$. A 2D front (zero level set) in (**a**) is propagated outwards, represented by the 3D level sets in (**b**), (**c**) and (**d**), respectively

one dimension higher than the original (i.e. a 2D contour is represented as zero level set of a 3D function). Instead of tracing the interface itself, the level set method builds the original curves (so-called front) into a level set surface ϕ (a hyper surface), where the front propagates with a speed F in its normal direction. To avoid complex contours, the current front $\phi(x, y, t = i)$ is always set at zero height $\phi = 0$ as depicted in Fig. 2. Hence, the level set evolution equation for the moving hyper surface can be presented as a Hamilton–Jacobi equation:

$$\phi_t + F|\nabla\phi| = 0. \tag{1}$$

The benefit of employing this "one-dimension-higher" concept is that even though the front (zero level set $\phi = 0$) can become wildly contorted, the level set surface ϕ will always be well- behaved. All the complicated problems of contour breaking and merging are more easily handled in this environment. A full discussion of these concepts is beyond the scope of this paper; instead the reader is referred to [22] or Sethian's instructional web page.[1]

The level set method is designed for problems in which the speed function can be positive in some places and negative in others, so that the front can move both forwards and backwards.

The fast marching method [22] is a special case of the level set approach. Suppose, we now restrict ourselves to the particular case of a front propagating with a speed F, which is either always positive or always negative. This restriction allows us to simplify level set formulation. If we assume $T(x, y)$ be the time when the curve crosses the point (x, y), the surface $T(x, y)$ satisfies an Eikonal equation where the gradient of surface ∇T is inversely proportional to the speed of the front F:

$$|\nabla T|F = 1. \tag{2}$$

The fast marching method is designed for problems in which the speed function never changes sign, so that the front is always moving forward or backward and the front crosses each pixel point only once. This restriction makes the fast marching approach much more rapid than the more general level set method.

With respect to a rapidly computing segmentation result, we employ the fast marching method in our approach to perform the initial propagation of a contour from a user-defined seed to an approximate boundary.Aspeed term $gI(x, y, z)$ is computed based on image gradients and applied to the front, which forces it to stop near object boundaries:

$$g_I(x, y, z) = \frac{1}{1 + |\nabla(G_\sigma * I(x, y, z)|}. \tag{3}$$

In the above, $G_\sigma * I$. I denotes the convolution of the image with a Gaussian smoothing filter with standard deviation. The term $\nabla(G_\sigma * I(x, y, z))$ is essentially zero except when the image gradient changes rapidly, in which case the value becomes large and the propagation speed approaches zero.

---

[1] http://math.berkeley.edu/~sethian/Explanations/level_set_explain.html

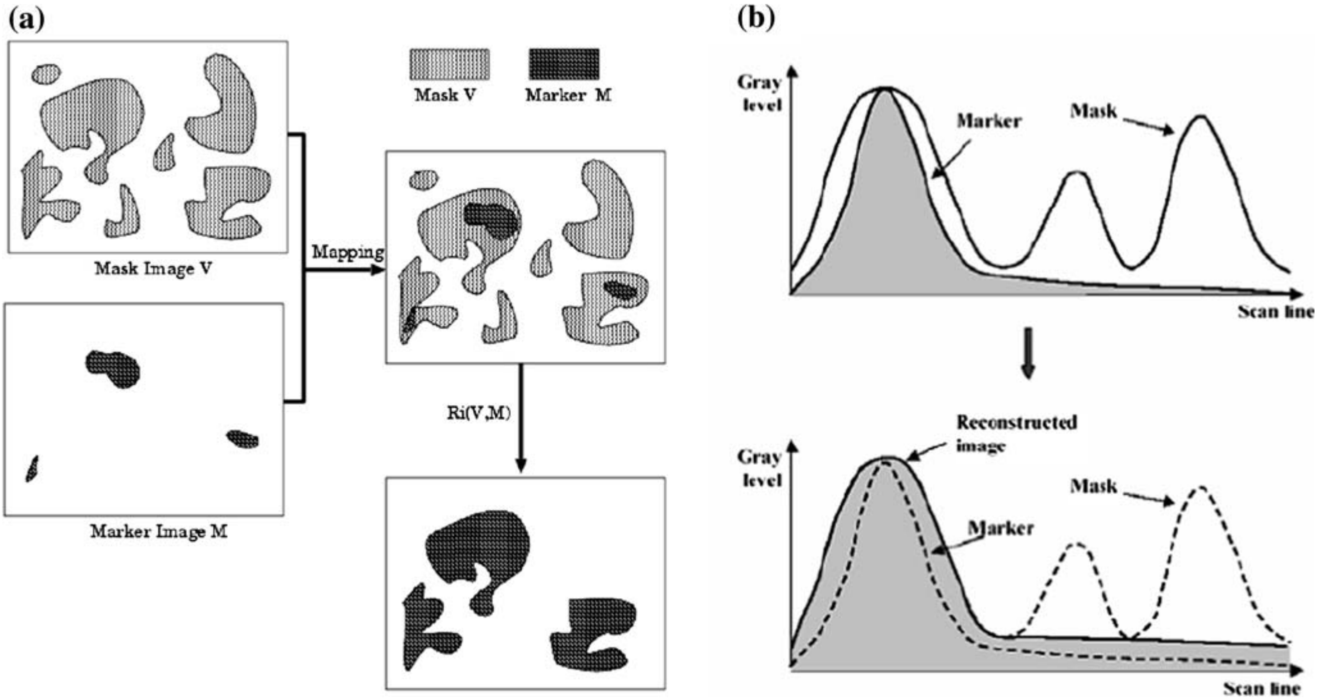

Fig. 3 Morphological reconstruction where regions in marker image are used to select regions of the mask image to be reconstructed. **a** The processing in a 2D binary image. **b** The procedure along a simple scan-line of a gray scale image

Morphological reconstruction

Mathematical morphology is a powerful methodology for the quantitative analysis of geometrical structures. It consists of a collection of theoretical concepts, nonlinear signal operators, and algorithms aiming at extracting objects from images. We employ the standard technologies of recursive erosion, recursive dilation, and morphological grayscale reconstruction in this research. More details can be found in [23,24].

We define a 3D image f as a subset of the 3D Euclidean space ($f \in \mathbf{R}^3$), and a 3D structuring element $k \in \mathbf{R}^3$. The four basic operations can be defined as follows:

Dilation:

$$f \oplus k = \bigcup_{b \in k} (\{a + b | a \in f\}), \tag{4}$$

Erosion:

$$f \ominus k = \bigcap_{b \in k} (\{a - b | a \in f\}), \tag{5}$$

Opening:

$$f \circ k = (f \ominus k) \oplus k, \tag{6}$$

Closing:

$$f \bullet k = (f \oplus k) \ominus k. \tag{7}$$

Recursive dilation, recursive erosion, and morphological reconstruction [8] defined below are based on these four basic operations:

Recursive dilation:

$$F \overset{i}{\oplus} K = \begin{cases} F & \text{if } i = 0 \\ (F \overset{i-1}{\oplus} K) \oplus K & \text{if } i \geq 1, \end{cases} \tag{8}$$

Recursive erosion:

$$F \overset{i}{\ominus} K = \begin{cases} F & \text{if } i = 0 \\ (F \overset{i-1}{\ominus} K) \ominus K & \text{if } i \geq 1 \end{cases} \tag{9}$$

Morphological reconstruction:

$$B_i = (B_{i-1} \oplus_g k) \cap |f|_G \left(B_i \in R^3, i = 1, 2, \ldots \right) \tag{10}$$

In the above, i is a scale factor and K is the basic structuring element (e.g. 1 pixel radius disk). $\oplus_{\mathrm{g}}$ denotes a dilation operation in grayscale, and $|f|_{\mathrm{G}}$ represents the mask of the operation, achieved via a threshold operation using a gray level G. The iteration in (10) is repeated until there is no further change between B_{i-1} and B_i.

Recursive erosion is employed here to reduce connectivity of objects from neighboring tissues while recursive dilation recovers the region lost during the reduction after the objects have been totally segmented. Each step employs the same number of iterations N.

Morphological reconstruction is a very accurate and efficient tool for recovering the object on a pixel-by-pixel basis. The seed, which results from the output of the fast marching algorithm, is recursively grown under the supervision of the mask until it converges to a stable shape. Morphological reconstruction operations on both binary and grayscale images are depicted in Fig. 3.

Multistage hybrid segmentation approach

Our 3D segmentation algorithm is a multistage procedure, which is composed of four major stages (Fig. 1):

Stage 1 Reduce the connectivity between the object region and the neighboring tissues. Recursively erode the input 3D image using a structuring element base (e.g. a sphere with 1 pixel radius) until the desired object region is completely separated from the neighboring tissues, as determined by the operator. Record the iteration number N for later use in stage 3. This step is designed to prevent overflow during the propagation in stages 2 and 3.

Stage 2 Perform initial evolution of the front.The fast marching method is employed here to initially propagate the userdefined seed to a position close to the boundary. It performs rapidly, typically less than 20 s for a 256 × 256 × 100 volume, running on a 550 MHz Dual PIII-based personal computer.

Stage 3 Refine the contours created in stage 2. Since the speed function in the fast matching method falls to zero sharply, the front could stop a few voxels away from the real boundary. Here, a grayscale morphological reconstruction algorithm is employed to refine the front as a “final check”. The output from stage 2 is employed as marker, while the original image is used for the mask.

Stage 4 Recover the lost data elements from stage 1. During the recursive erosion in stage 1, part of the object (usually around the edges) is also often eliminated. To recover these lost components, the recursive dilation method is employed. The reconstructed object surface is dilated recursively using the same number of iterations N as recorded in stage 1, which results in the recovery of the object surface to the “original” position.We note that the resultant image will not in general exactly correspond to the “original” image, but be smoothed, since erosion, followed by dilation corresponds to an “opening” operation. It nevertheless removes most of the noise surrounding the desired boundary. However, if we use a sphere with 1 pixel radius as the structuring element, and employ a small number of iterations to reduce the connectivity, the surfaces of smooth convex structures may be recovered accurately.

Finally, the segmented result may be visualized by either surface or volume-rendering methods.

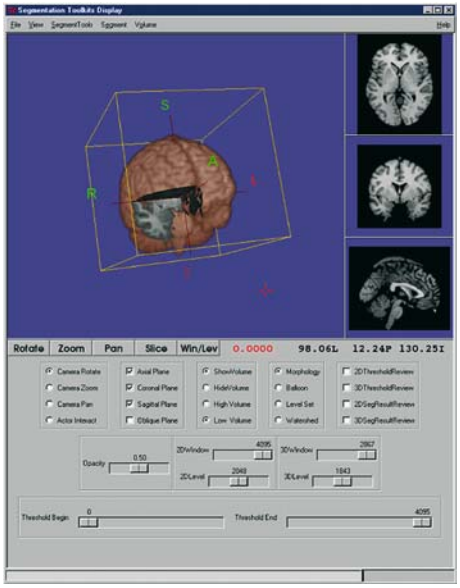

● Camera Rotate
○ Camera Zoom
○ Camera Pan
○ Actor Interact

☑ Axial Plane
☑ Coronal Plane
☑ Sagittal Plane
☐ Oblique Plane

● ShowVolume
○ HideVolume
○ High Volume
● Low Volume

● Morphology
○ Balloon
○ Level Set
○ Watershed

☐ 2DThresholdReview
☐ 3DThresholdReview
☐ 2DSegResultReview
☐ 3DSegResultReview

Opacity 0.50
2DWindow 4095
2DLevel 2048
3DWindow 2867
3DLevel 1843
Threshold Begin 0
Threshold End 4095

Fig. 4 A snapshot of the user-interface to control the segmentation software and visualize its results

Experimental results

Software and source data

We developed a segmentation environment, “TkSegment”, based on the visualization toolkit (VTK) and the Python language, into which our multistage hybrid segmentation algorithm was integrated. The user-interface of the package is shown in Fig. 4.

The source data employed in our experiments include 60 CT or MRI datasets from brain, heart, and kidney studies. One of the 5 brain MRI datasets is the standard CJH27 image volume derived from an average of 27 T1 weighted images of a normal brain [25]. We also employed this volume in the validation study described later. CJH27 is a $181 \times 217 \times 181$ voxel volume, with isotropic 1 mm^3 voxels. The other four T1- or T2-weighted neurological MRI datasets are $256 \times 256 \times 124$ volumes. Five groups of canine CT datasets were employed for the cardiac study. Each was a dynamic volume, acquired with a gated acquisition technique on an 8-slice GE helical CT scanner, consisting of 86 slices at each of 10 equally spaced snapshots during the cardiac cycle. The images were 512 × 512 pixels (0.35mm×0.35mm), each with an axial spacing of 1.25 mm. Five CT datasets were employed in the kidney example. These volumes comprised 512 × 512 (0.5 mm^2) pixels per slice, and 130 slices spaced by 1.25 mm.

We applied our segmentation algorithm to these 60 volume datasets. A Pentium III 550 MHz dual CPU desktop computer running MS-windows NT was employed to run the segmentation. The results of these experiments are described below.

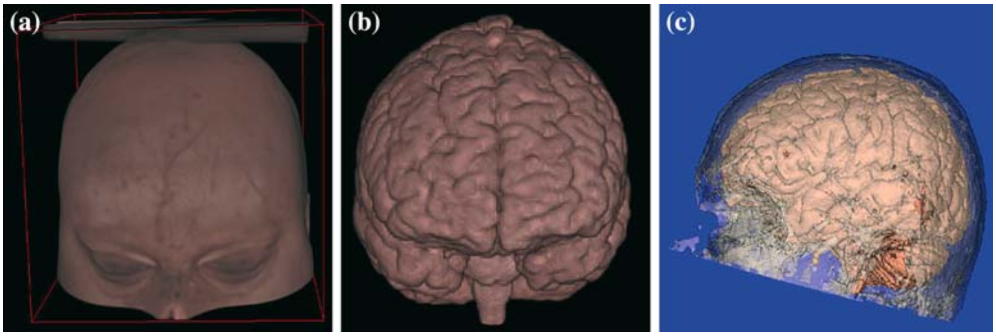

Fig. 5 Examples of CJH27 brain where the source (**a**) is segmented to (**b**) (volume rendered), and segmented brain with its transparent skull is shown as (**c**) (surface rendered)

Case study

Brain images We applied our algorithm to five MRI T1 or T2 head scans. One of the volumes (CJH27) is shown in Fig. 5a. The segmentation result is shown in Fig. 5b, and the segmented brain associated with its transparent skull is shown in Fig. 5c.

The segmentation procedure was applied to all the five scans. The average computing timewas 38 s for each volume. We considered this to be sufficiently rapid to classify as "near real time" segmentation. The accuracy of the segmentation result is discussed below in Sect. Validation.

Heart images Five dynamic CT scans of beating hearts, each containing ten individual volumes throughout the cardiac cycle, were used in this study. Each of the ten images was segmented individually. Although the segmentation of a beating heart is more difficult than a brain due to the more complex anatomy as well as the presence of the artifacts and non-isotropic image resolution, our hybrid approach handled these data in a robust manner – in spite of such potential problems. Examples of the segmented results are shown in Fig. 6a and b which represent the segmented volume of diastolic and systolic phases, respectively.

The average segmentation time for one of these volumes is 215 s, which is significantly longer than for the brain, due to the additional time required to segment the blood vessels. However, if the blood vessels are removed early in pre-processing, computational time reduces dramatically to 46 s.

Kidney images For the kidney example, we employed five CT datasets to test our approach. At the second stage (fast marching as illustrated in Fig. 2), we initiated the procedure using a separate seed in each kidney to speed up the processing. After the process was initiated, the resulting fronts in both kidney regions propagated independently and concurrently. Fig. 7a shows a pair of kidneys associated with the vessels, while Fig. 7b displays the kidneys surrounded by ribs and spine.

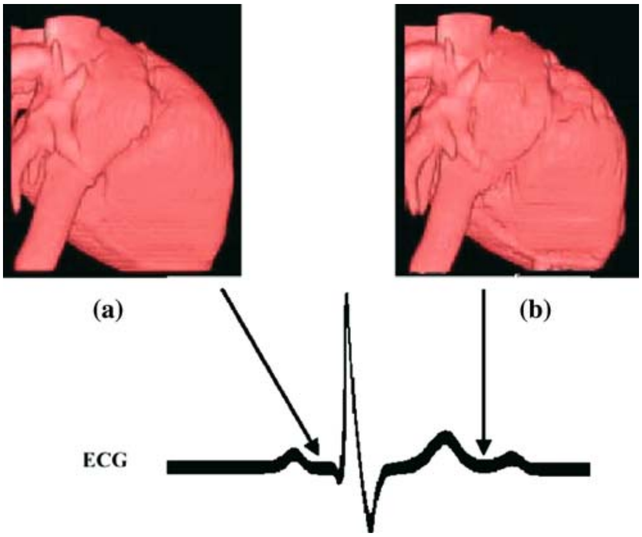

Fig. 6 Examples of two of the ten segmented heart volumes in a cardiac cycle. **a** Diastolic phase. **b** Systolic phase

The average segmentation time for kidneys alone is 23 s (e.g. Fig. 7b). However, if the propagation processing includes the renal vessel system, the time typically increases to approximately 280 s (e.g. Fig. 7a).

From the results of these experiments, we can conclude that, in terms of providing satisfactory artifact-free segmented results, our hybrid algorithm is robust across a range of typical clinical image datasets.

Validation

The segmentation results on the 60 experimental datasets were examined by our clinical colleagues and deemed to be sufficiently accurate for the purposes of further medical applications.

Three volumes were chosen for quantitative validation. CJH27 (Fig. 7) was selected from the neurological image group because it forms the basis of a simulated MR dataset for which "ground-truth" is known. This standard brain was

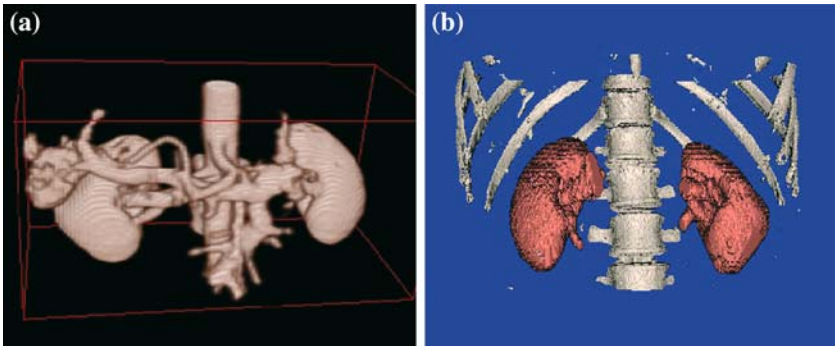

Fig. 7 Examples of the segmented kidney. **a** Apair of kidneys associated with vessels (volume rendered). **b** Apair of kidneys associated with ribs and spine (surface rendered)

generated from a set of 3D "fuzzy" anatomical models [25]. Each model represents a typical tissue class (white matter, gray matter, CSF, etc.). This model was then used as input for a MR simulator[2] that produces a realistic MR volume image for which "ground-truth" is known with respect to its components. Other volumes were chosen from cardiac and kidney datasets. For the latter two examples, contours manually traced by an expert were employed as the gold standard.

To quantify the segmented results, we used the similarity index definition introduced by Zijdenbos [26], which is related to a reliability measure method known as the kappa statistic. Consider C1 and C2 as a segmented result and the gold standard, respectively. The similarity between C1 and C2 is given by $S \in [0, 1]$ and defined as:

$$S = \frac{2N(C_1 \cap C_2)}{N(C_1) + N(C_2)}. \qquad (11)$$

Here $N(\mathrm{C})$ is the number of pixels included in the binary image C. This index is sensitive to the size of both the images (C1 and C2) and their relative locations. $S = 0$ indicates no overlap, while $S = 1$ represents a perfect agreement. Zijdenbos states that $S > 0.7$ indicates excellent agreement. The relationship between the separation of two volume surfaces and the similarity index can be described by the following simple example. Assume a sphere volume C1 with radius 100 voxels (similar to a brain volume) and another sphere volume C2 with a radius of 99 voxels. The similarity index between these two volumes is $S = 0.97$.

The total error between the gold standard and the automatically segmented result is 0.037 measured on the basis of the similarity index, i.e. $S = 0.963$. The main differences between them are distributed in four areas, which are color coded and shown in Fig. 8. Red, blue, green, and orange represent the regions of non-overlap between the two images, of blood vessels in the sagittal sinus, edges of the frontal lobes, brainstem, and edges of cerebellum, respectively. Most of the differences were found in the area of the sagittal sinus, which accounts for 73% of the error. While most of these vessels were carefully excluded from the gold standard, our automatic segmentation procedure included them as part of the brain. Even though there are only a small number of voxel differences at one location at the edges of the frontal lobe, this source nevertheless accounts for 21% of the errors, due to the large surface area of the lobe. The third source of error occurs at the edges of the cerebellum, accounting for 4% while 2% of error occurs at the bottom of the brainstem.

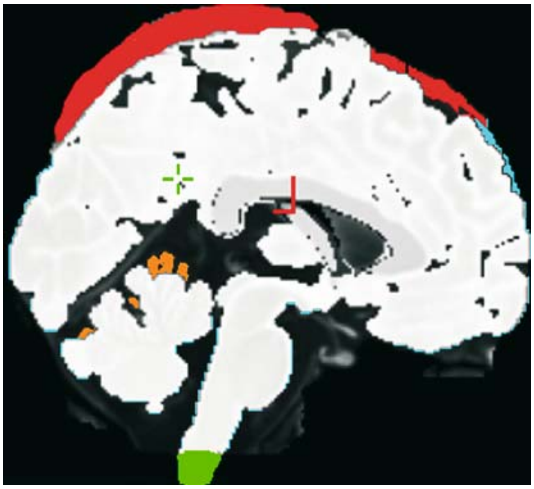

Fig. 8 Error distribution between two volumes. *Color* coded regions are the difference between (*a*3) and (*b*3) indicating the errors in the area of blood vessel in the sagittal sinus (*red*), edges of the frontal lobe (*blue*), edges of cerebellum (*orange*), and brainstem (*green*)

The sagittal sinus area was the only part of the brain that was over-segmented, as seen in Fig. 8. The frontal lobe edges, cerebellum, brainstem, and a small vascular area were all under-segmented. One cause of the under-segmentation is the strict setting of the halting criterion of the propagation to prevent the over-segmentation. Another reason is that the gold standard not only includes white and gray matter, but also includes CSF, which was excluded in our segmentation.

The similarity indicies of the experimental results are shown in Table 1. The CJH27 brain achieved a similarity index of 0.963. The validation results from other two volumes are quite similar to the result with CJH27, with a similarity index of 0.956 being obtained from the heart segmentation and a 0.978 being obtained from the kidney study. The average index across all modalities was 0.966.

---

[2] http://www.bic.mni.mcgill.ca/brainweb/.

Table 1 The similarity index of the experimental results

Dataset	Gold standard (voxels)	Auto result (voxels)	Similarity index
CJH27	25,62,601	25,33,055	0.963
Heart	26,37,084	26,71,856	0.956
Kidney	8,86,123	8,85,649	0.978
Average	–	–	0.966

Discussion

This approach achieves highly accurate segmentation results for a variety of input datasets. Our method identifies and reconstructs the structure of the organ for high quality visualization across a variety of conditions, even in the imperfect world of routine clinical-quality images. Additionally, we believe that it represents the first near real time, full 3D segmentation approach tested in different application areas. The discussion below focuses on two aspects of the algorithm – its robustness and performance including executing time and accuracy.

Robustness

Robustness of the multistage hybrid segmentation approach was tested by 60 medical datasets in both MRI and CTmodalities. As described in Sect. Validation, the segmentation results of the multi-modality datasets were found to be of sufficient quality for medical visualization and other medical applications in the area of image-guided surgery and therapy, computer-aided diagnosis and robotically-assisted surgery. Both research data and clinical data were employed in our validation experiments, and no failed segmentations were reported even in low quality clinical images. Apart from the CJH27 dataset, all of the employed datasets were typical diagnostic-quantity clinical images. Note that while the cardiac images were obtained from a research study using dogs, the scan protocol was similar to that employed for human studies.

Performance

Model-based methods, such as active contour algorithm can perform "real time" segmentation in 2D slice processing, where the segmentation results are usually sufficiently accurate for specific applications. Region-based segmentation methods such as conventional region-growing methods or morphological operation can achieve a highly accurate segmentation result, but require more computational times.Based on our test using VTK's built-in algorithms and running in the same computing environment, morphological operations alone require 8 min to segment CJH27 brain.MacDonald [17] presented a deformable surface method to extract inner and outer surfaces of cerebral cortex. His approach achieved a high quality brain surface model, but required 30 h of time on a Silicon Graphics Origin 200 workstation running at 180 MHz. Compared to the existing algorithms, we believe that our hybrid approach represents a significant improvement.

As described in the Introduction section, our hybrid approach has been optimized for 3D volume segmentation. It combines the speed advantage of model-based methods with the high accuracy of region-based methods, resulting in an algorithm that is both fast and accurate, which was validated by our experiments achieving an average similarity index of 0.966.

Conclusion

We presented above a new fully 3D, precise, reliable segmentation approach for visualization using a fast multistage hybrid algorithm. The approach takes advantage of the speed and accuracy of both model-based and region-based segmentation methods. It was tested on 60 3D image volumes in a variety of application studies and image modalities, demonstrating excellent segmentation results. Quantitative validation demonstrated an average accuracy of 0.966, measured on the basis of a similarity index.

While the procedure currently requires a minimal userinteraction to place seeds, and to identify the stopping criterion at the erosion stage, we propose to improve the algorithm to make it fully automatic. We are considering the morphological "Top-hat" transformation [27], which can extract regions of high intensity of similar size to the objects to be segmented. The detected regions can then be employed as initial seeds. This step is still quite computational expensive, and we therefore chose not to use it in our current work.

As demonstrated by the dramatic increase in segmentation speed when vascular structures were removed from our volumes, the segmentation of vessels remains a bottleneck. We believe that dealing with vessels separately, using skeleton techniques [24], in place of the fast marching algorithm, could significantly improve the efficiency of this step.

Acknowledgements The authorswould like to thank Pencilla Lang for her great help in validation of the segmentation approaches described in this paper. We are also grateful to Dr. Colin Holmes for providing his CJH27 brain; to the Montreal Neurological Institute for the use of BrainWeb; to David Gobbi for software support; and to Drs.Yves Starreveld, John D. Denstedt, James D.Watterson, and Darren T. Beiko for providing us with image data and evaluating the segmentation results. The paper is partially supported by the NSFC research fund (60571061) and STCSM international research fund (45107045).

References

1. Bedzek JC, Hall LO, Clarke LP (1993) Review of MR image segmentation techniques using pattern recognition. Med Phys 20(4):1033.1048
2. Frangi AF, Niessen WJ, Viergever MA (2001) Three-dimensional modeling for functional analysis of cardiac images:AReviewIEEE Trans Med Imaging 20(1):2.25
3. Awcock GJ, Thomas R (1996) Applied image processing. McGraw-Hill, New York
4. Rajapakse JC, Giedd JN, Rapopart JL (1997) Statistical approach to segmentation of single-channel cerebralMRimages. IEEE Trans Med Imaging 16(2):176–186
5. Kass M, Witkin A, Terzopolous D (1988) Snake: active contour models. Int J Compt. Vis 1:321–331
6. Osher S, Sethian JA (1988) Fronts propagating with curvature dependent speed: algorithms based on Hamilton.Jacobi formulation. J Comput Phys 79:12–49
7. Sekiguchi H, Sano K, Yokoyama T (1994) Interactive 3-dimensional segmentation method based on region growing method. Syst Comput Jp 25(1):88–97
8. Vincent L (1993) Morphological grayscale reconstruction in image analysis: applications and efficient algorithms. IEEE Trans Image Process 2(2):176–201
9. Vincent L, Soille P (1991)Watersheds in digital spaces: an efficient algorithm based on immersion simulations. IEEE Trans Pattern Anal Mach Intell 13(6):583–598
10. Cheng F, Venetsanopoulos AN (2000) Adaptive morphological operators fast algorithms and their aplications. Pattern Recognit 33:917–933
11. Bieniek A, MorgaA(2000) An efficient watershed algorithm based on connected components. Pattern Recognit 33:907–916
12. Gu L, Peters T (2004) Robust 3D organ segmentation using a fast hybrid algorithm. In: Proceedings of 18th international congress and exhibition on computer assisted radiology and surgery(CARS2004), pp. 69–74, June 2004
13. Yezzi A, Kichenassamy S, Kumar A, Olver P, Tannenbaum A (1997) A geometric snake model for segmentation of medical imagery . IEEE Trans Med Imag 16(2):199–209
14. Atkins MS, Mackiewich BT (1998) Fully automatic segmentation of the brain in MRI. IEEE Trans Med Imaging 17(1):98–107
15. Audette MA, Peters TM (1999) Level-set segmentation and registration for computing intrasurgical deformations. In: Proceedings of SPIE 3661 medical imaging 1999, pp 110.121
16. Bomans M, Hohne K-H (1990) 3D Segmentation of MR images of the head for 3D display. IEEE Trans Med Imaging 9(2):177–183
17. Macdonald D, Kabani N, Avis D, Evans AC (2000) Automated 3D extraction of inner and outer surfaces of cerebral cortex from MRI. NeuroImage 12:340–356
18. Snel JG, Venema HW, Grimbergen CA (2002) Deformable triangular surface using fast 1-D radial lagrangian dynamics . segmentation of 3D MR and CT image of the wrist. IEEE Trans Med Imaging 21(8):888–903
19. Chalana V, Linker DT, Haynor DR, Kim Y (1996) A multiple active contour model for cardiac boundary detection on echocardiograpgic sequences. IEEE Trans Med Imaging 15(3):290–298
20. Choi SM, Lee JE, Kim J, Kim MH (1997) Volumetric object reconstruction using the 3D-MRF model-based segmentation. IEEE Trans Med Imaging 16(6):887–892
21. Leemput KV, Maes F, Vandermeulen D, Suetens P (1999) Automated model- based tissue classification of MR images of the brain. IEEE Trans Med Imaging 18(10):897–908
22. Sethian JA (1999) Level set methods and fast martching methods. Cambridge University Press
23. Serra J (1982) Image analysis and mathematical morphology. Academic Press, London, U.K.
24. Haralick RM, Shapiro LG (1992) Computer and robot vision. vol 1, Addison-Wesley Press, Reading
25. Kwan RKS, Evans AC, Pike GB (1999) MRI simulation-based evaluation of image processing and classification methods. IEEE Trans Med Imaging 18(11):1085–1097
26. Zijdenbos AP, Dawant BM,Margolin RA, Palmer AC (1994) Morphometric analysis of white matter lesions in MR images: method and validation. IEEE Trans Med Imaging 13:716–724
27. Gu L, Kaneko T (2000) Extraction of organs using threedimensional mathematical morphology. Syst Comput Jpn 31(7):29–37